12th International Symposium on Turbulence and Shear Flow Phenomena (TSFP12)
Osaka, Japan (Online), July 19-22, 2022

LOW-ORDER REPRESENTATION OF THE WAKE DYNAMICS OF OFFSHORE FLOATING WIND TURBINES

Cédric Raibaudo, Laurent Perret
LHEEA
Centrale Nantes
1 Rue de la Noë, 44300 Nantes, France
cedric.raibaudo@univ-orleans.fr

ABSTRACT

A low-order representation of the wake downstream a porous disk modeling a wind turbine is considered here. Synchronized Stereo-PIV measurements and hot-wire anemometry are performed to accurately represent the wake flow dynamics. Realistic flow conditions are generated, ensuring a proper scaling of the incoming boundary layer and the wind turbine. The porous disk can also translate along the longitudinal direction to simulate realistic surge-motion of a floating wind turbine. The velocity fields are reconstructed at higher temporal resolution using POD and multi-time delay Linear Stochastic Estimation, for the characterization of the full dynamics of both the boundary layer and the wake flow developing downstream of the model. The surge-motion imposed on the model shows to have a significant influence on the flow dynamics, in particular on the temporal modes of the POD decomposition.

INTRODUCTION

For the recent years, fixed and floating offshore wind turbine have been of particular interest from both scientific and industrial communities. A full understanding of wind turbines wakes is crucial to improve their aerodynamical performances when operating in wind farms (Schmidt & Stoevesandt, 2015; Bastine *et al.*, 2018). The optimization of offshore wind farms is important as the space with wind resources is limited. For offshore wind turbines embedded in wind farms, multiple dynamics and phenomena impact the wake characteristics, including the influence of the incoming atmospheric boundary layer, the wake dynamics itself and the effect of the wave-induced surge-motion. In particular, the influence of the surge-motion due to the structure movement of a floating wind turbine, and the consideration of a realistic turbulent boundary layer have recently been touched on (Fu *et al.*, 2019; Schliffke *et al.*, 2020; Wise & Bachynski, 2020). Even if large-eddy simulation (LES) approaches have been employed increasingly in the previous years for these complex modes, the computational cost of these simulations is still prohibitive for practical applications (Bastine *et al.*, 2018).

For onshore wind turbines, wake models exist in the literature (Heemst, 2015). Simple models are based on the velocity deficit, which could include turbine additional turbulence and wake meandering (Jensen, 1983; Ainslie, 1988; Frandsen *et al.*, 2006). More complex wake models have been developed using CFD (Frandsen *et al.*, 2006), but they are considered lacking of physical representativity compared with experimental studies and full CFD. Low-order representation of the wake, less costly and capable of reproducing the full physical phenomena, is therefore preferred. For this objective, modal decomposition has been used to determine low-dimensional model of the turbulent wind field (Bastine *et al.*, 2018, 2015; Hamilton *et al.*, 2018; Sarmast *et al.*, 2014; Saranyasoontorn & Manuel, 2005). Proper Orthogonal Decomposition (POD) is, in particular, a well-known method to extract the most energetic coherent structures in the flow (Sirovich, 1987). For example, POD has been applied for wakes of an infinitely long row of wind turbines (Andersen *et al.*, 2014).

For floating wind turbines, modal decomposition was not much suggested yet. POD analysis was performed on generated wind fields using Mann and Kaimal turbulence models (Bachynski & Eliassen, 2019), or by associating LES simulations (Nybø *et al.*, 2020). However, available synthetic turbulence models for generating these inflow conditions for simulations codes for performance and loads estimation are currently unable to account for all these interactions. Therefore, being able to model the complex dynamics of the wind turbine wake flow interacting with the atmospheric boundary layer to provide unsteady aeroelastic computational codes with realistic inlet conditions is of crucial importance.

The objective of the present study is to show the potential and validity of a low-order representation of the flow obtained from synchronized hot-wire anemometry (HWA) and Particle Image Velocimetry (PIV) measurements performed in the wind tunnel to accurately represent the wake flow dynamics. To this aim, realistic flow conditions are generated within the wind tunnel, ensuring that the incoming boundary layer and the wind turbine modeled by a porous disk are properly scaled. In addition, the porous disk can also translate along the longitudinal direction to mimic realistic surge-motion of a floating wind turbine. The velocity fields are reconstructed at high temporal resolution using a dimensionality reduction and reconstruction approach based on both POD and multi-time delay Stochastic Estimation, allowing for a detailed characterization of the dynamics of both the incoming boundary layer and the wake flow developing downstream of the model.

EXPERIMENTAL SET-UP

Experiments were carried in the LHEEA's atmospheric wind tunnel. The experimental set-up is presented in Fig. 1. The wind turbine is modeled using a porous disk of diameter $D = 0.16$ m. The disk center is set at a height $z_{hub} = 0.12$ m with respect to the floor. The model represents the floating

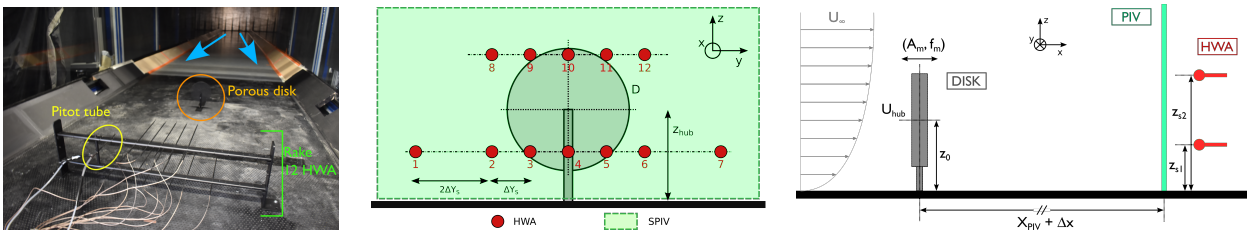

(a) (b)

Figure 1. Experimental set-up: (a) picture of the set-up in the wind-tunnel and (b) schemes of the set-up.

2MW wind turbine used in the FLOATGEN research project, installed at Centrale Nantes' offshore test site in Le Croisic, France. The thrust coefficient C_t is estimated to be approximately 0.5 and the power coefficient $C_p \approx 0.25$ (Schliffke *et al.*, 2020). For streamwise positions x/D in the wake further than 3, the use of porous disks for the characterization of wind turbines wakes is considered valid (Schliffke *et al.*, 2020). Without model, the free-stream velocity is $U_\infty = 4.2$ m/s and the turbulent intensity about 0.5%. The incoming boundary layer thickness is $\delta = 0.6$ m and the resulting Reynolds number is $Re = U_\infty \delta / \nu \approx 150000$.

To replicate realistic behaviors of floating wind turbines under wave swell, a sinusoidal surge-motion is imposed on the model using a linear actuator (Schliffke *et al.*, 2020). The sinusoidal amplitude is $\pm$ 0.01 *m* and the frequencies tested $f_m = [0,\ 2,\ 3,\ 3.75]$ *Hz*. The model position is controlled retroactively and monitored, with a bias of about 1 *mm* between the expected and real positions (Schliffke *et al.*, 2020).

The wake is characterized with Stereoscopic PIV (SPIV or PIV 2D3C) in a $y-z$ plane normal to the main flow direction at two streamwise positions $x/D = 4.6$ and 8.1 downstream of the wind turbine model. The range of the final region of interest is about $3D \times 2D$ along these directions. The sampling frequency is $f_{PIV} = 14.1$ Hz and 14000 snapshots were acquired for each case. Constant temperature anemometry (CTA) measurements were also performed simultaneously to the Stereo-PIV. Twelve HWA sensors are distributed spanwise, downstream the PIV measurement plane and at two heights (0.47D and 1.25D). The sampling frequency for the HWA is $F_{HWA} = 15$ kHz. Sensors were calibrated using a King's law by measuring the free-stream flow with the help of a Pitot tube. These HWA acquisitions were considered, in addition to the wake documentation with means statistics and spectral analysis, to perform the linear stochastic estimation of time-resolved velocity fields.

MEAN FLOW

The present study is first used to document the mean flow without model and the wake. The mean and RMS velocities of the atmospheric turbulent boundary layer without model are presented in Fig. 2. Profiles of the three components along the wall-normal direction z/D going through the disk center ($y/D = 0$) are considered here. Mean streamwise velocity $\overline{U}/U_\infty$ corresponds to a turbulent boundary layer profile and from previous works in this wind tunnel (Schliffke *et al.*, 2020). A small negative spanwise velocity $\overline{V}/U_\infty \approx 1$ % is also observed for the turbulent boundary layer. It has been observed in previous works and could be linked to large flow structures developing upstream the measurement region.

The comparison of the turbulence intensities with the German VDI requirements (VDI, 2017), already applied by Schliffke *et al.* (2020) for the current turbulent boundary layer, is

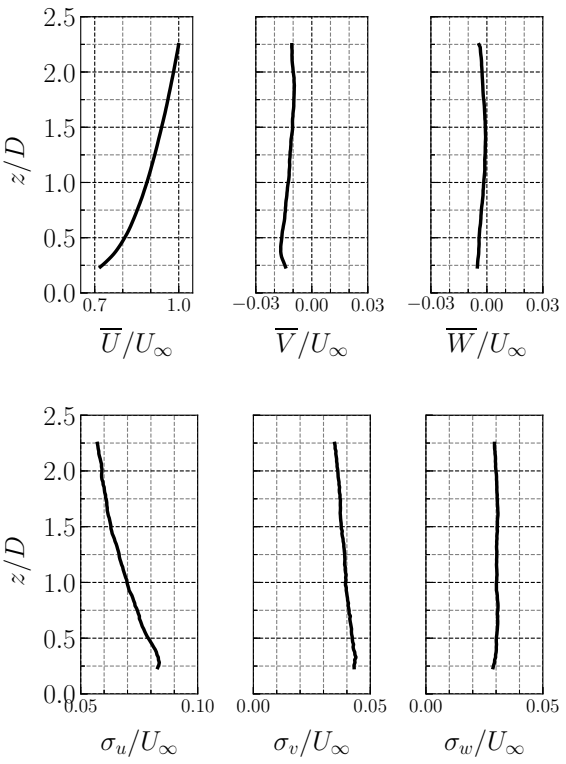

Figure 2. Mean $\overline{U}/U_\infty$ (first line) and RMS velocities σ_u/U_∞ (second line) at $y/D = 0$ for the three spatial components for the turbulent boundary layer without model. Scales are significantly different between the streamwise velocity and the other velocity components.

also valid for the 1 / 750 scaled model. The streamwise turbulence intensity I_u fits well with the VDI database, when the spanwise and wall-normal components I_v and I_w are underestimated by a third.

The mean wake flow is also documented with these measurements. Streamwise mean and RMS velocity fields are presented in Fig. 3. Two streamwise positions in the wake are presented here: $x/D = 4.6$ and 8.1. The mean flow in the near-wake is disturbed by the disk, following its shape (represented with dash line in Fig. 3). At $x/D = 8.1$, the wake center is slightly shifted to the negative y-direction, also seen in previous works (Schliffke *et al.*, 2020; Foti *et al.*, 2019). It could correspond to the small spanwise velocity of the incoming flow observed previously. Compared to the flow without model, the turbulence intensity increases in the near-wake from 8 % up to 15 %. The circular horseshoe shape in the near-wake has been found in previous works (Hamilton *et al.*, 2018). The slight shift in the negative y-direction is observed to the RMS fields

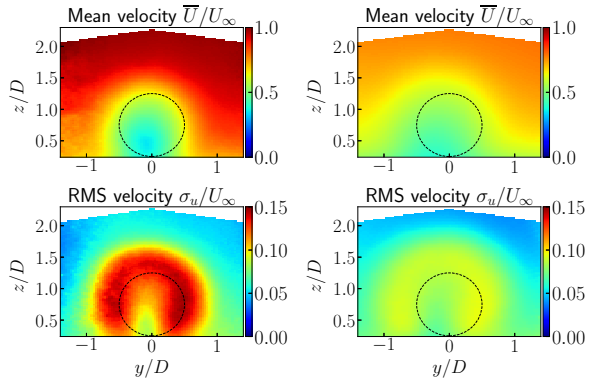

(a) $X/D = 4.6$ (b) $X/D = 8.1$

Figure 3. Streamwise mean $\overline{U}/U_\infty$ (first line) and RMS velocity σ_u/U_∞ (second line) for: (a) wake for the fixed model at $x/D = 4.6$ and (b) wake for the fixed model at $x/D = 8.1$. Dash lines correspond to the position of the porous disk in the $Y-Z$ plane.

at $x/D = 8.1$.

METHODOLOGY OF THE RECONSTRUCTION USING POD-mLSE

Spatial velocity fields measured by PIV and synchronized time-resolved velocity measurements using HWA are combined for the reconstruction of the full spatio-temporal dynamics using a multi-time-delay Proper Orthogonal Decomposition and Linear Stochastic Estimation (POD-mLSE) approach (Durgesh & Naughton, 2010). Velocity fields are decomposed into temporal and spatial modes using the classical snapshots POD:

$$\mathbf{u}(\mathbf{x},t) \approx \sum_{i=0}^{N_m} a_i(t)\, \Phi_i(\mathbf{x}) \tag{1}$$

with N_m the number of modes selected for the truncature. Here, $N_m = 100$ modes are chosen, corresponding to about 80% of the cumulative eigenvalues energy. The objective is to determine the more suitable coefficients B_{ijk} to express the relation between the temporal modes a_i and the HWA sensors with time delays τ_k:

$$a_i(t) = \sum_{j=0}^{N_j} \sum_{k=0}^{N_k} B_{ijk}\, S_j(t-\tau_k) \tag{2}$$

with $N_j = 12$ the number of HWA sensors S_j and N_k the number of delays imposed on the sensors. Here, $N_k = 21$ delays are distributed between ± 1 s, following previous reconstruction parameters on similar experiments (Blackman & Perret, 2016). The coefficients B_{ijk} are determined through the resolution of a least-square minimization problem using cross-correlations:

$$B_{ijk} \;=\; \mathscr{C}^{-1}_{\{a_i,\, S_{jk}\}}\, \mathscr{C}_{\{S_{jk}\}} \tag{3}$$

with $\mathscr{C}_{\{a_i,\, S_{jk}\}}$ the cross-correlations between the temporal modes and the sensors with delays, and $\mathscr{C}_{\{S_{jk}\}}$ the correlations between the different sensors with different delays. Temporal modes $\widehat{a}_i$ are therefore estimated at higher temporal resolution using Eq. 2, then combined with the spatial modes using POD (Eq. 1) to reconstruct the velocities. Two flow configurations considered for reconstruction are presented here, as important cases for their implementation in aeroelastic simulations: the turbulent boundary layer alone and the fixed model wake immersed in the turbulent boundary layer at $x/D = 8.1$. The sampling frequency used for the reconstruction is $F_s = 7.05$ kHz, to meet the conditions required for these simulations.

POD MODES

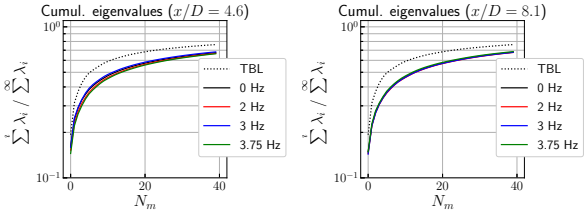

(a) (b)

Figure 4. Cumulative eigenvalues $\sum_i^i \lambda_i / \sum_i^\infty \lambda_i$ from the POD obtained from different streamwise positions (a) $x/D = 4.6$ and (b) $x/D = 8.1$. For each configuration, four frequencies of motion f_m are presented in solid lines: 0 Hz (fixed), 2 Hz, 3 Hz and 3.75 Hz. TBL without model is presented in dotted line.

The main results of the POD analysis are presented here. The convergence using the cumulative eigenvalues $\sum_i^i \lambda_i / \sum_i^\infty \lambda_i$ is first shown in Fig. 4. The two streamwise positions in the wake are considered, and compared with the POD modes for the turbulent boundary layer without model. Compared with typical bluff-body flows, the eigenvalues convergence is relatively slow, due to the high Reynolds number incoming turbulent boundary layer. The eigenvalues are therefore comparable with previous works, in particular De Cillis *et al.* (2021): for a near-wake flow downstream a nacelle and tower model, the cumulative eigenvalues reached about 40 % after $N_m = 15$ modes, as it is about 50 % for the present study for the same amont of modes.

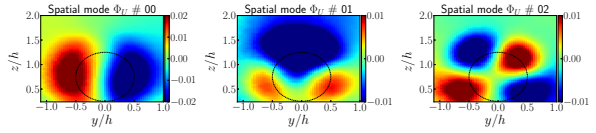

Figure 5. Example of spatial modes Φ_i maps for modes $i =$ 0 to 2 (*columns*) for the fixed model ($f_m = 0$ Hz) at $x/D = 4.6$.

An example of the spatial modes Φ_i is presented in Fig. 5. The dipole-like pairs (modes 0 and 1, oriented respectively in the spanwise and wall-normal direction) and quadripole-like pairs (mode 2 and 3, not shown here), are similar to the ones obtained for similar configurations (Andersen *et al.*, 2013; Bastine *et al.*, 2014). The symmetry of modes pairs corresponds to an invariance of the flow under rotations (Berkooz *et al.*, 1993; Bastine *et al.*, 2014). However, symmetry of the

mode 1 is slightly broken in the wall-normal due to the incoming boundary layer, which is not always taken into account in studies.

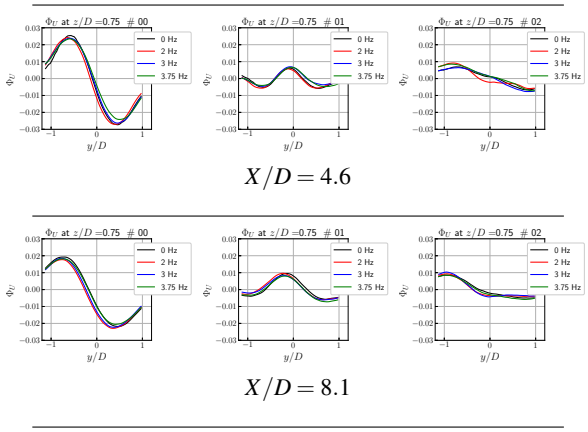

Figure 6. Profiles of spatial modes Φ_i for two streamwise positions and along the spanwise y direction at the hub height $z/D = 0.74$ for modes $i = 0$ to 2 (Raibaudo *et al.*, 2022).

Profiles of the spatial modes Φ_U of the streamwise velocity component for two streamwise positions and along the spanwise y-direction are presented in Fig. 6. Profiles are considered at the hub height ($z/D = 0.74$) and for different frequencies of surge-motion. Modes signs are adapted for a better comparison. A more complete analysis of the POD modes for the floating wind turbine can be found in Raibaudo *et al.* (2022). No significant influence of the surge-motion can be found in the spatial modes. Profiles are close in amplitude and shape. Same observations can be performed for the other velocities components v and w.

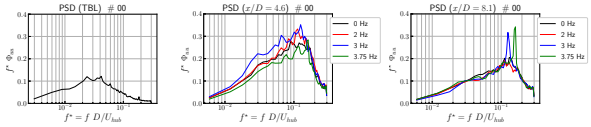

Figure 7. Premultiplied PSD of the temporal modes a_i obtained from different configurations: (a) turbulent boundary layer without model, (2) model wake at $x/D = 4.6$ and (3) model wake at $x/D = 8.1$ (Raibaudo *et al.*, 2022).

However, as detailed in Raibaudo *et al.* (2022), significant differences can be observed on the temporal modes. Premultiplied PSD of the temporal modes a_i are presented in Fig. 7 for three configurations (TBL and the two streamwise positions in the wake). Non-dimensionalized frequency $f^* = fD/U_{hub}$ is used here to dimensionalize the PSD, as performed in previous works, with $U_{hub} = 3.8$ m/s the velocity at the hub position without model.

A broad spectrum is found for the flow without model, centered around the main reduced frequency ($f^* = 0.04$ or $f \approx 1$ Hz). By considering the porous disk wake without motion, the spectra amplitude increases significantly and the main frequency is shifted to $f^* = 0.13$ ($f \approx 3$ Hz). Eventually, the surge-motion imposes the dynamics of the wake. In particular, the higher surge-motion frequencies have a greater influence on the wake. For example, a motion at frequency $f_m = 2$ Hz shows similar dynamical behavior than the fixed model, where motions of $f_m = 3$ and 4 Hz shows the emergence of substantial peaks and increase of the spectral energy at low frequency.

RECONSTRUCTION

Few results of the reconstruction of the velocity fields are presented here. Only the turbulent boundary layer and the far-wake for the fixed model are shown here, but the stochastic estimation was performed for the full database.

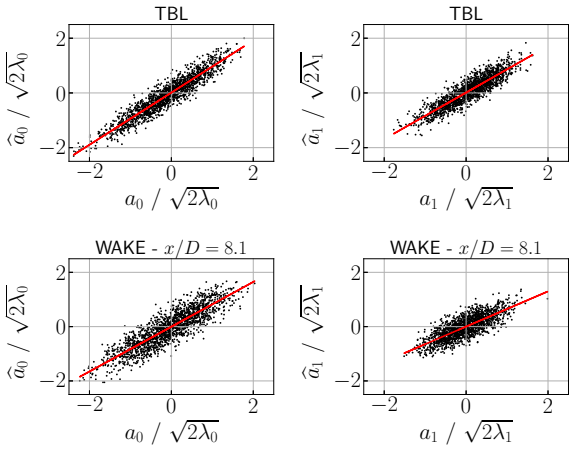

Figure 8. Scatter plots for the first two reconstructed temporal mode $\widehat{a}_i/\sqrt{2\lambda_i}$ versus original mode $a_i/\sqrt{2\lambda_i}$ at two streamwise positions: (a-b) turbulent boundary layer without model, (c-d) $x/D = 8.1$.

A first comparison of the first reconstructed temporal modes $\widehat{a}_i/\sqrt{2\lambda_i}$, with λ_i the POD eigenvalue of mode i, is performed in Fig. 8. These reconstructed modes $\widehat{a}_i$ are compared to the original modes a_i: strong correlation is observed for both chosen configurations, suggesting the reconstruction is consistent. It can be observed the distribution is more scattered for the reconstruction of the wake than for the turbulent boundary layer, implying more difficulties to capture the flow complexity of the wake.

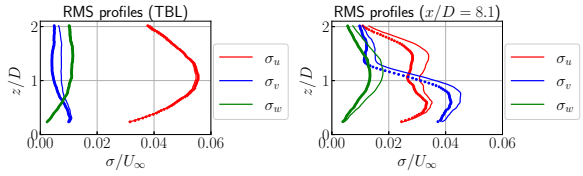

Figure 9. RMS reconstructed velocity u/U_∞ profiles along z using mtd-POD-LSE and original velocity using the same amount of modes $N_m = 100$. (a) TBL and (b) fixed model at $x/D = 8.1$. dots: truncated original PIV data, lines: mtd-POD-LSE data

Reconstructed RMS velocity profiles along z are shown in Fig. 9. These reconstructed velocities are compared with the original velocities obtained by the POD truncature (Eq. 1)

with the same amount of modes $N_m = 100$ used for the mtd-POD-LSE process. For the turbulent boundary layer (Fig. 9 (a)), the streamwise and normal terms, respectively u/U_∞ and w/U_∞, are well reconstructed. Only the spanwise component v/U_∞ is underestimated of about 30% in average over the profile, more importantly far from the wall. Same analysis can be done for the reconstruction of the model wake at $x/D = 8.1$ (Fig. 9 (b)). All reconstructed velocities components are consistent with the original velocities. However, the reconstructed velocities are underestimated between 4% for u/U_∞ to 15% for w/U_∞. Even if the stochastic estimation looses information similarly to the TBL, these differences could be linked to the conditioning of the correlation matrix during the POD process and could be improved by using Tikhonov regularization for example. The presence of the model generates a more pronounced three-dimensional wake which is captured by the SPIV but not well by the one-dimensional hot-wires.

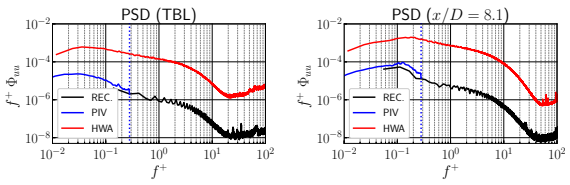

Figure 10. Premultiplied PSD of the reconstructed velocities at the hub position, compared to the PIV and HWA. (a) TBL and (b) fixed model at $x/D = 8.1$. The vertical dashed line corresponds to the PIV sampling frequency limit.

Spectral analysis is also performed on the reconstructed streamwise velocity and presented in Fig. 10. PSD are compared with the ones done with the original velocity with the same amount of modes and on a hot-wire sensor ($n°10$ at $y/D = 0$ and $z/D = 1.25$). Spectrum is consistent at low frequency with the PIV and follows well the dynamics behavior of hot-wire sensor. A loss of spectrum amplitude is also observed between the two, suggesting a loss of information at higher frequency with the process due to the POD truncature and the limited number of sensors, for example.

PSD of the reconstructed velocities are also consistent with the spectral analysis on the PIV and HWA. Spectra have more amplitude at low frequency, with peaks at $f^+ = \mathcal{O}(10^{-1})$, and reconstructed velocity PSDs also catch this behavior at lower frequency.

CONCLUSIONS AND PERSPECTIVES

Considering realistic conditions of the incoming flows of wind turbines has been proven to be of crucial importance. In the present study, velocity fields have been obtained experimentally for the turbulent boundary layer and wakes of fixed and moving porous disk corresponding to realistic behaviors of offshore wind turbines. The velocity has been reconstructed at high temporal resolution using mtd-POD-LSE. The influence of the surge-motion on the POD modes has been presented here, and detailed in a previous article. The spatial modes show no significant difference due to the motion, when the temporal modes includes the spectral signature of the surge-motion. In particular, higher surge-motion frequencies shows the emergence of strong peaks on the PSDs. Spatio-temporal dynamics of the wake flow has been shown to be well captured by this low-order representation of the turbulent flow.

The reconstructed fields will now be implemented in an aero-elastic code for the estimation of the forces applied on the real scale wind turbine. Not detailed here, but during the presentation and in a future publication, the influence of the high-frequencies surge-motions of the floating wind turbine will strongly impact the mean and RMS forces obtained with these calculus. The importance of a realistic flow dynamics consideration for the study of floating wind turbines is therefore confirmed.

REFERENCES

Ainslie, J.F. 1988 Calculating the flowfield in the wake of wind turbines. *Journal of Wind Engineering and Industrial Aerodynamics* **27** (1-3), 213–224.

Andersen, Søren Juhl, Sørensen, Jens Nørkær & Mikkelsen, Robert 2013 Simulation of the inherent turbulence and wake interaction inside an infinitely long row of wind turbines. *Journal of Turbulence* **14** (4), 1–24.

Andersen, S. J., Sørensen, J. N. & Mikkelsen, R. 2014 Reduced order model of the inherent turbulence of wind turbine wakes inside an infinitely long row of turbines. *Journal of Physics: Conference Series* **555** (1).

Bachynski, Erin E. & Eliassen, Lene 2019 The effects of coherent structures on the global response of floating offshore wind turbines. *Wind Energy* **22** (2), 219–238.

Bastine, David, Vollmer, Lukas, Wächter, Matthias & Peinke, Joachim 2018 Stochastic wake modelling based on POD analysis. *Energies* **11** (3), 1–29.

Bastine, D., Witha, B., Wächter, M. & Peinke, J. 2014 POD analysis of a wind turbine wake in a turbulent atmospheric boundary layer. *Journal of Physics: Conference Series* **524** (1).

Bastine, David, Witha, Björn, Wächter, Matthias & Peinke, Joachim 2015 Towards a simplified dynamic wake model using POD analysis. *Energies* **8** (2), 895–920.

Berkooz, Gal, Holmes, Philip & Lumley, John L 1993 ProOrthDecHydroAnnurev1993.pdf. *Annual Review of Fluid Mechanics* (25), 539–575.

Blackman, Karin & Perret, Laurent 2016 Non-linear interactions in a boundary layer developing over an array of cubes using stochastic estimation. *Physics of Fluids* **28** (9).

De Cillis, Giovanni, Cherubini, Stefania, Semeraro, Onofrio, Leonardi, Stefano & De Palma, Pietro 2021 POD-based analysis of a wind turbine wake under the influence of tower and nacelle. *Wind Energy* **24** (6), 609–633.

Durgesh, V. & Naughton, J. W. 2010 Multi-time-delay LSE-POD complementary approach applied to unsteady high-Reynolds-number near wake flow. *Experiments in Fluids* **49** (3), 571–583.

Foti, Daniel, Yang, Xiaolei, Shen, Lian & Sotiropoulos, Fotis 2019 Effect of wind turbine nacelle on turbine wake dynamics in large wind farms. *Journal of Fluid Mechanics* **869**, 1–26.

Frandsen, Sten, Barthelmie, Rebecca, Pryor, Sara, Rathmann, Ole, Larsen, Søren, Højstrup, Jørgen & Thøgersen, Morten 2006 Analytical modelling of wind speed deficit in large offshore wind farms. *Wind Energy* **9** (1-2), 39–53.

Fu, Shifeng, Jin, Yaqing, Zheng, Yuan & Chamorro, Leonardo P. 2019 Wake and power fluctuations of a model wind turbine subjected to pitch and roll oscillations. *Applied Energy* **253** (February), 113605.

Hamilton, Nicholas, Viggiano, Bianca, Calaf, Marc, Tutkun, Murat & Cal, Raúl Bayoán 2018 A generalized framework for reduced-order modeling of a wind turbine wake. *Wind*

Energy **21** (6), 373–390.

Heemst, Johannes Willem Van 2015 Improving the Jensen and Larsen Wake Deficit Models .

Jensen, N O 1983 A note on wind generator interaction. *Risø-M-2411 Risø National Laboratory Roskilde* pp. 1–16.

Nybø, Astrid, Nielsen, Finn Gunnar, Reuder, Joachim, Churchfield, Matthew J. & Godvik, Marte 2020 Evaluation of different wind fields for the investigation of the dynamic response of offshore wind turbines. *Wind Energy* **23** (9), 1810–1830.

Raibaudo, Cédric, Piquet, Thibaud, Schliffke, Benyamin, Conan, Boris & Perret, Laurent 2022 POD analysis of the wake dynamics of an offshore floating wind turbine model. *Journal of Physics: Conference Series* .

Saranyasoontorn, Korn & Manuel, Lance 2005 Low-dimensional representations of inflow turbulence and wind turbine response using Proper Orthogonal Decomposition. *Journal of Solar Energy Engineering, Transactions of the ASME* **127** (4), 553–562.

Sarmast, Sasan, Dadfar, Reza, Mikkelsen, Robert F., Schlatter, Philipp, Ivanell, Stefan, Sørensen, Jens N. & Henningson, Dan S. 2014 Mutual inductance instability of the tip vortices behind a wind turbine. *Journal of Fluid Mechanics* **755**, 705–731.

Schliffke, Benyamin, Aubrun, Sandrine & Conan, Boris 2020 Wind Tunnel Study of a "floating" Wind Turbine's Wake in an Atmospheric Boundary Layer with Imposed Characteristic Surge Motion. *Journal of Physics: Conference Series* **1618** (6).

Schmidt, Jonas & Stoevesandt, Bernhard 2015 The impact of wake models on wind farm layout optimization. *Journal of Physics: Conference Series* **625** (1).

Sirovich, Lawrence 1987 Turbulence and the dynamics of coherent structures. Part 1: Coherent structures. *Quarterly of Applied Mathematics* **15** (3), 561–571.

VDI 2017 Environmental meteorology - Turbulence parameters for dispersion models supported by measurement data. *Tech. Rep.*. Verein Deutscher Ingenieure.

Wise, Adam S. & Bachynski, Erin E. 2020 Wake meandering effects on floating wind turbines. *Wind Energy* **23** (5), 1266–1285.